Radical Doping Hot Paper

How to cite: *Angew. Chem. Int. Ed.* **2020**, *59*, 19087–19094
International Edition: doi.org/10.1002/anie.202005012
German Edition: doi.org/10.1002/ange.202005012

Expanded Analogs of Three-Dimensional Lead-Halide Hybrid Perovskites

*Daiki Umeyama, Linn Leppert, Bridget A. Connor, Mary Anne Manumpil, Jeffrey B. Neaton, and Hemamala I. Karunadasa**

Abstract: *Replacing the Pb–X octahedral building unit of $A^{I}PbX_3$ perovskites (X = halide) with a pair of edge-sharing Pb–X octahedra affords the expanded perovskite analogs: $A^{II}Pb_2X_6$. We report seven members of this new family of materials. In 3D hybrid perovskites, orbitals from the organic molecules do not participate in the band edges. In contrast, the more spacious inorganic sublattice of the expanded analogs accommodates larger pyrazinium-based cations with low-lying π* orbitals that form the conduction band, substantially decreasing the band gap of the expanded lattice. The molecular nature of the conduction band allows us to electronically dope the materials by reducing the organic molecules. By synthesizing derivatives with A^{II} = pyridinium and ammonium, we can isolate the contributions of the pyrazinium-based orbitals in the band gap transition of $A^{II}Pb_2X_6$. The organic-molecule-based conduction band and the inorganic-ion-based valence band provide an unusual electronic platform with localized states for electrons and more disperse bands for holes upon optical or thermal excitation.*

[*] Dr. D. Umeyama, B. A. Connor, Dr. M. A. Manumpil, Prof. H. I. Karunadasa
Department of Chemistry, Stanford University
Stanford, CA 94305 (USA)
E-mail: hemamala@stanford.edu

Dr. D. Umeyama
International Center for Materials Nanoarchitectonics, National Institute for Materials Science
1-1 Namiki, Tsukuba, Ibaraki 305-0044 (Japan)

Dr. L. Leppert
Institute of Physics, University of Bayreuth
95440 Bayreuth (Germany)

Prof. J. B. Neaton
Molecular Foundry, Lawrence Berkeley National Laboratory
Berkeley, CA 94720 (USA)
and
Department of Physics, University of California Berkeley
Berkeley, CA 94720 (USA)
and
Kavli Energy NanoScience, Institute at Berkeley
Berkeley, CA 94720 (USA)

Prof. H. I. Karunadasa
Stanford Institute for Materials and Energy Sciences, SLAC National Accelerator Laboratory
Menlo Park, CA 94025 (USA)

Supporting information and the ORCID identification number(s) for the author(s) of this article can be found under: https://doi.org/10.1002/anie.202005012.

Introduction

Hybrid materials offer the potential of coupling the electronic properties of covalent organic molecules and ionic inorganic solids. Diverse organic molecules have substantially expanded the functionality of hybrids such as organic-inorganic nanocomposites,[1] periodic mesoporous organosilicates,[2] and metal-organic frameworks.[3] In the family of hybrid halide perovskites, two-dimensional (2D) derivatives can hold aliphatic and aromatic molecules of a wide range of sizes between the inorganic sheets.[4] As a result, the quantum-well-like electronic structure of 2D hybrid perovskites can be manipulated by tuning the relative energy levels of the organic and inorganic components.[5] In contrast, the diversity of organic molecules that can be accommodated in the 3D perovskite lattice is severely limited by the small size of the cuboctahedral cavity defined by the inorganic lattice. For example, the 3D perovskite $APbI_3$ is known to house only $CH_3NH_3^+$ and $(H_2N)_2CH^+$ as stoichiometric A-site organic cations.[6] Small amounts (ca. 20%) of slightly larger cations such as ethylammonium and guanidinium are reported to fit in the A-site only when mixed with $CH_3NH_3^+$ cations.[7] In order to access the greater electronic diversity seen in 2D perovskites,[8] while exhibiting 3D connectivity that would provide wider band dispersion compared to the 2D lattices, we explored methods of expanding the 3D perovskite lattice.

Herein, we show that the perovskite lattice can be expanded by replacing PbX_6^{4-} octahedra with a $Pb_2X_{10}^{6-}$ dimer of edge-sharing octahedra as the basic building unit. These dimers share corners to extend in all three dimensions. The expanded inorganic sublattice can be derived from the perovskite lattice by translating alternating slices cut along the (110) crystallographic plane in order to form edge-sharing dimers of Pb–X octahedra (Figure 1). The expanded anionic inorganic sublattice in $A'Pb_2X_6$ incorporates larger organic A′-site cations, including aromatic molecules whose π* orbitals can participate in the band edges. A similar approach to lattice expansion has been previously used in the closely related Prussian blue lattice, where $M(CN)_6^{n-}$ (M = divalent or trivalent metal) octahedral building units have been replaced by larger molecular clusters terminating with cyanides that maintain octahedral symmetry.[9]

A series of pyrazinium-based A′-site dications afford the 3D expanded perovskite analogs $A'[Pb_2X_6]$ with A′ = dmpz (*N*, *N*′-Dimethylpyrazinium), Hmpz (*N*-Hydro-*N*′-methylpyrazinium), Hepz (*N*-Hydro-*N*′-ethylpyrazinium), Hppz (*N*-Hydro-*N*′-isopropylpyrazinium) and X = I or Br (Figure 2). These organic dications indirectly and directly affect the

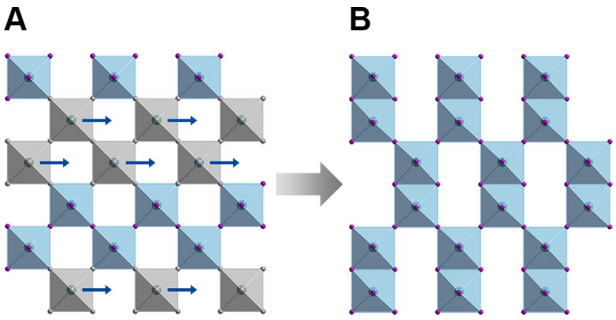

Figure 1. Conceptual transformation of the inorganic sublattice from A) a 3D perovskite to B) its expanded analog, where the lead-halide octahedra in A) are replaced with edge-sharing dimers of octahedra in B). Lead and halide atoms are represented as turquoise and purple spheres, respectively.

valence and conduction bands, respectively. Templating effects by the organic cations induce different degrees of distortion in the lead-halide lattice, altering the dispersion of the valence band that is composed of lead and halide orbitals. On the other hand, the low-lying π* orbitals of the pyrazinium cations compose the conduction band and the band gap transition takes the form of a charge transfer from the inorganic to the organic sublattice. The distinctly molecular nature of the conduction band allows us to dope the materials by using organic radicals for the self-assembly reaction. To confirm participation of pyrazinium orbitals in the band edges of these new materials, we also synthesized analogous lattices with pyridinium and ammonium dications: H_2apy (*N*,*N*′-Dihydro-3-amidinopyridinium), and H_2dap (*N*,*N*′-Dihydro-1,3-propanediammonium). Here, the unoccupied orbitals of the organic dications are higher in energy compared to those of pyrazinium. Indeed, A′[Pb_2X_6] with A′ = H_2apy and H_2dap show similar band gap orbital makeup as for typical halide perovskites. The 2D analog of this lattice is known,[10] and just prior to submission of this paper, 3D lattices with edge-sharing octahedra with a different connectivity were reported.[11] The organic cations in these reported lattices, aminomethylpyridinium and 2-trimethylammonioethylammonium, do not contribute orbitals to the band edges, in contrast to the pyrazinium-based lattices described here.

Results and Discussion

Combining PbX_2 (X = Br or I) and the halide salts of the organic cations in organic solvents containing LiX or NaX (to provide an excess of X^- in solution) or aqueous HX solutions afforded the A′[Pb_2X_6] family of expanded perovskite analogs (see Supporting Information for detailed procedures). For X = Br, six analogs were synthesized (Figure 2) with A = dmpz (**1**Br), Hmpz (**2**Br), Hepz (**3**Br), Hppz (**4**Br), H_2apy (**5**Br), and H_2dap (**6**Br) as dark red (**1**Br-**4**Br), pale-yellow (**5**Br), or colorless (**6**Br) crystals. For X = I, one analog was synthesized with A = dmpz (**1**I) as opaque black crystals. Crystals suitable for single-crystal X-ray diffraction were obtained for all samples. Solid **2**Br crystallizes with some iodide as (Hmpz)[$Pb_2Br_{4.5}I_{1.5}$] and attempts to synthesize the pure bromide were not successful. The phase purity of all powder samples was confirmed by powder X-ray diffraction (PXRD, Supporting Information, Figures S1–S7).

Water stability

Powders of (Hmpz)[Pb_2Br_6] (**2**Br), (Hepz)[Pb_2Br_6] (**3**Br) and (Hppz)[Pb_2Br_6] (**4**Br) are moisture sensitive and gradually change color under ambient humidity. In contrast, powders of (dmpz)[Pb_2X_6] (**1**Br and **1**I) show surprisingly

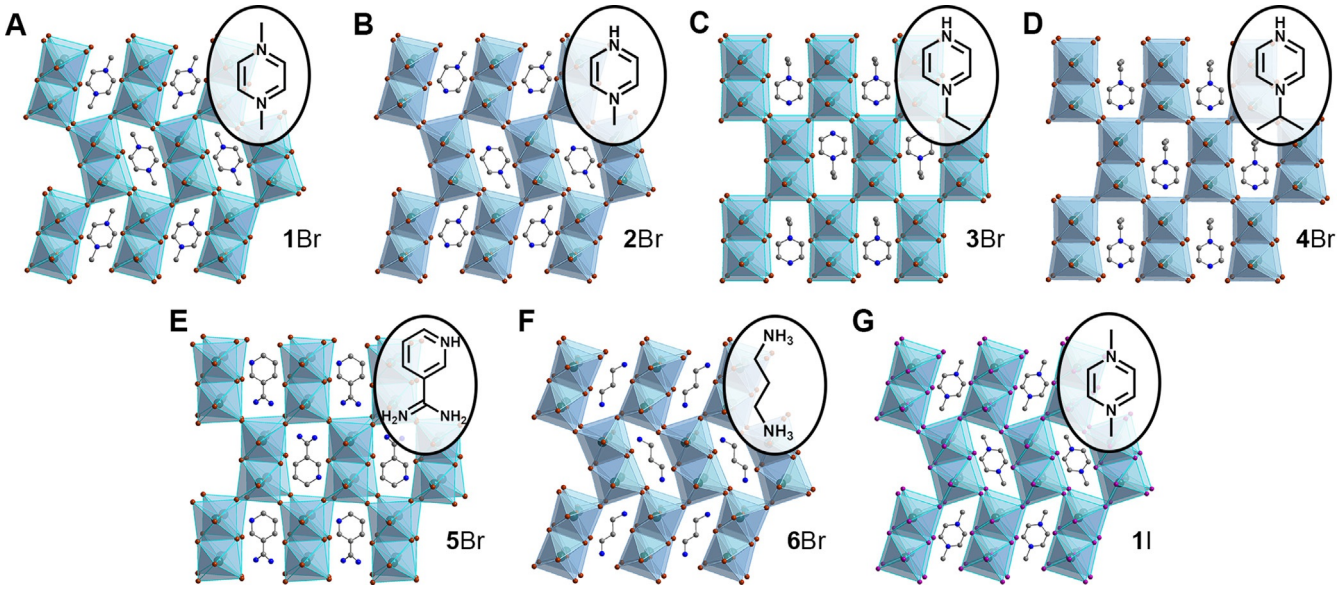

Figure 2. Single-crystal X-ray crystal structures of A) (dmpz)[Pb_2Br_6] (**1**Br), B) (Hmpz)[Pb_2Br_6] (**2**Br), C) (Hepz)[Pb_2Br_6] (**3**Br), D) (Hppz)[Pb_2Br_6] (**4**Br), E) (H_2apy)[Pb_2Br_6] (**5**Br), F) (H_2dap)[Pb_2Br_6] (**6**Br), and G) (dmpz)[Pb_2I_6] (**1**I). Turquoise, purple, brown, blue, and gray spheres represent Pb, I, Br, N, and C atoms, respectively. Disordered atoms and H atoms are omitted for clarity. The organic dications are shown in the insets.

greater moisture resistance. Solid (dmpz)[Pb_2I_6] (**1I**) does not decompose even when immersed in water, maintaining phase purity, as determined through PXRD, after the powder was stirred in water for 90 minutes at room temperature (Figure 3 A,B). The salt (dmpz)(BF_4)$_2$ is highly water soluble, and changes color from violet to black (Supporting Information, Figure S8) when dissolved in water, which has been ascribed to radical-mediated decomposition of the dmpz cations.[12] Peaks corresponding to PbI_2, the decomposition product, were observed in the PXRD data only after **1I** was stirred in hot water (70 °C) for 2 h (Figure 3 B). The water stability of **1I** is notably greater than that of the perovskite (CH_3NH_3)PbI_3, which decomposes immediately when immersed in water and in several hours upon exposure to moist air.[13] Because **2**Br, **3**Br, and **4**Br with *N*-bound protons on the pyrazinium rings are more water sensitive than **1**Br and **1I**, which do not contain acidic protons, the initial steps of the decomposition may involve deprotonation of pyrazinium cations by water molecules. Indeed, the pK_a values of pyrazinium cations are sufficiently low to protonate water molecules.[14]

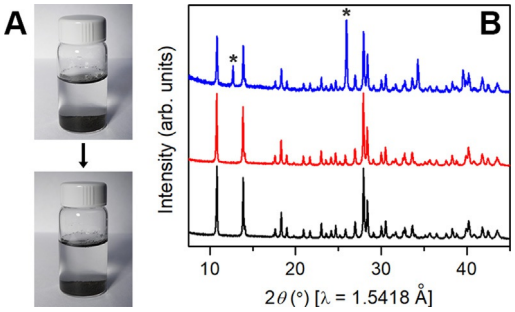

Figure 3. A) Photographs of (dmpz)[Pb_2I_6] (**1I**) powder in water at ambient temperature at $t = 0$ minutes (top) and $t = 90$ minutes (bottom). B) Powder X-ray diffraction (PXRD) patterns of **1I**: as synthesized (black), after stirring in water for 90 minutes at room temperature (red), and after stirring in water for 2 h at 70 °C (blue). Asterisks denote peaks corresponding to PbI_2.

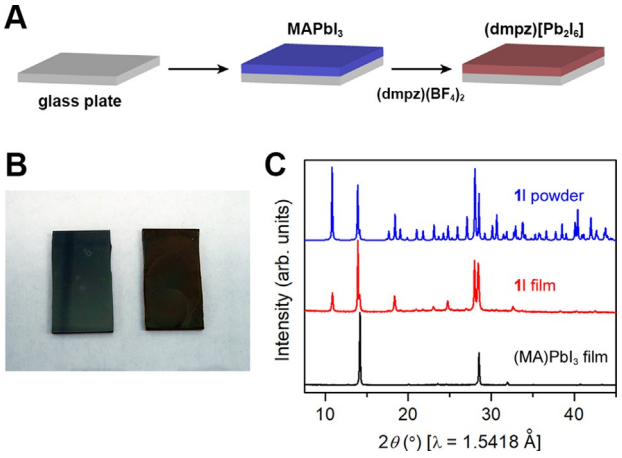

Figure 4. A) Film deposition procedure for **1I** (B) Photographs of the films of (MA)PbI_3 (left; MA = $CH_3NH_3^+$) and **1I** (right). C) PXRD patterns of a (MA)PbI_3 film (black) and a converted film (**1I**, red). A simulated PXRD pattern of **1I** is shown in blue.

Film deposition from solution

Because the water insolubility of (dmpz)[Pb_2I_6] (**1I**) makes film deposition from solution difficult, we developed a two-step procedure to form films. In the first step, a film of (CH_3NH_3)PbI_3 was spun on a glass substrate using a reported method.[15] Then a methanol solution of (dmpz)(BF_4)$_2$ was dropped on the (CH_3NH_3)PbI_3 film and annealed at 100 °C for two minutes to convert it to a film of **1I** (Figure 4 A,B). The PXRD pattern confirmed the complete conversion of (CH_3NH_3)PbI_3 to a film of **1I** with weak preferred orientation parallel to the (001) plane (Figure 4 C). The infrared spectrum of the **1I** film did not show the N-H bending mode at 1654 cm^{-1} or B-F stretch at 1060 cm^{-1}, suggesting that the residual (CH_3NH_3)BF_4 left the film during annealing (Supporting Information, Figure S9). The absorption onset of the film of **1I** determined through transmission spectroscopy appears at 1.4 eV (Supporting Information, Figure S10), consistent with the diffuse reflectance data obtained from the powder sample (Figure 5 A). Therefore, the water insolubility of **1I** does not preclude solution-state film deposition.

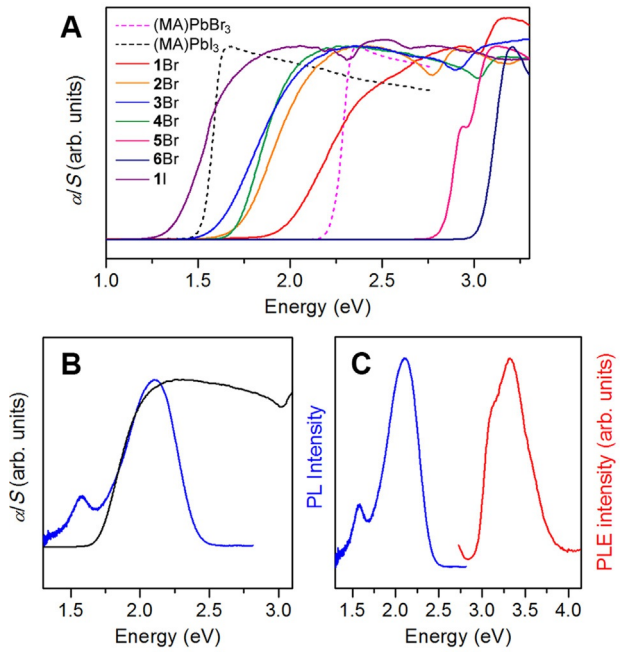

Figure 5. A) Diffuse reflectance data transformed using the Kubelka–Munk function (α and S are the absorption and scattering coefficients, respectively) for (dmpz)[Pb_2Br_6] (**1**Br; red), (dmpz)[Pb_2I_6] (**1I**; purple), (Hmpz)[Pb_2Br_6] (**2**Br; orange), (Hepz)[Pb_2Br_6] (**3**Br; blue), (Hppz)-[Pb_2Br_6] (**4**Br; green), (H_2apy)[Pb_2Br_6] (**5**Br; pink), (H_2dap)[Pb_2Br_6] (**6**Br; navy), respectively. Pink and black dashed lines represent (CH_3NH_3)$PbBr_3$ and (CH_3NH_3)PbI_3, respectively. B) Low-temperature photoluminescence (PL) spectrum of **4**Br at 25 K (blue line) overlaid with the diffuse reflectance data (black line). C) Photoluminescence excitation (PLE) spectrum at 80 K probing the emission from **4**Br at 2.1 eV overlaid with the low-temperature PL spectrum at 25 K (blue line).

Structure

The basic building unit of the inorganic sublattice of the expanded perovskite analogs consists of a pair of edge-sharing PbX_6 octahedra, which forms a 3D lattice by sharing corners with adjacent dimers. This inorganic lattice is reminiscent of the "4L" perovskite-like structures seen in oxides, where the cubic close-packing sequence of AO_3 layers found in perovskites alternates with a hexagonal close-packing sequence, affording a structure in which dimers of octahedra share corners to make a 3D lattice.[16] However, the dimers in these lattices are composed of face-sharing octahedra instead of the edge-sharing connectivity seen in the new materials reported here.

The organic dications in $A'Pb_2X_6$ occupy the cavity surrounded by 8 pairs of Pb–X octahedra, similar to the cuboctahedral A-site cavity enclosed by 8 Pb–X octahedra in $APbX_3$ perovskites. The organic cations are disordered in **2**Br, **3**Br, and **5**Br. Further, **4**Br and **5**Br adopt polar space groups, which may be of utility in ferroelectric applications. The size of the organic dications in $A'Pb_2X_6$ affects the degree of the distortion of the inorganic lattice. The largest deviation from linearity in the Pb-(μ-X)-Pb angle, which defines tilts between the pairs of octahedra, occurs in $(H_2dap)[Pb_2Br_6]$ (**6**Br) (140.5(1)°), whereas only a small distortion is seen in $(Hepz)[Pb_2Br_6]$ (**3**Br) (171.0(2)°). In hybrid perovskites, such flexibility in the inorganic lattice is more common in 2D lattices, where the charge density and steric requirements of the organic cations drive the distortion.[17]

Optical properties

Solids **1**Br-**4**Br show absorption onsets in the range from ca. 1.7 eV (**3**Br; A′ = Hepz) to ca. 1.9 eV (**1**Br; A′ = dmpz), whereas the iodide $(dmpz)[Pb_2I_6]$ (**1**I) shows an absorption onset around 1.4 eV (Figure 5 A; see Supporting Information for the method of estimating these onsets). These values are significantly smaller than the band gap energies of the 3D perovskites $(CH_3NH_3)PbBr_3$ (2.3 eV) and $(CH_3NH_3)PbI_3$ (1.6 eV). The lower-energy band gap of $A'Pb_2X_6$ (A′ = pyrazinium) compared to that of $APbX_3$ could arise from either the different connectivity in the inorganic lattice, or from contributions from the pyrazinium cations to the band edges.

The valence band of lead-halide perovskites consists mostly of halide p orbitals, with some lead s-orbital character, whereas the conduction band shows dominant lead *p*-orbital character. Thus, the band gap transition primarily corresponds to a ligand-to-metal charge transfer (LMCT). However, the LUMO in a conjugated aromatic molecule can be lower in energy than the lead-*p*-orbital band,[5b–e] resulting in a decrease in band gap as the LUMOs of the organic molecules form the material's conduction band. This leads to a ligand-to-ligand charge transfer (LLCT) as the band gap transition. Such transitions have been seen in lower-dimensional structures owing to the relatively large size of the organic molecules containing low-energy π* orbitals.[18]

To determine if the pyrazinium orbitals caused the band gap reduction in $A'Pb_2X_6$, we replaced pyrazinium with pyridinium and alkylammonium dications in the $A'Pb_2X_6$ lattice through the synthesis of **5**Br and **6**Br, respectively. Solids **5**Br and **6**Br are pale yellow and colorless, respectively, whereas their pyrazine-based analogs are dark red, implicating the organic sublattice in the band gap reduction. Indeed, **5**Br and **6**Br show higher absorption onsets compared to their pyrazinium-based Pb–Br analogs (Figure 5 A). The absorption onsets of **5**Br and **6**Br occur at ca. 2.8 eV and 3.1 eV, respectively, between the band gaps for typical 2D and 3D Pb–Br perovskites. Indeed, the 2D analogs of the 3D $A'Pb_2X_6$ lattices, containing H_2apy and *N*,*N*′-dihydro-histaminium as the cations, and another 2D Pb–Br lattice possessing both corner- and edge-sharing octahedra exhibit higher band gaps than their 2D-perovskite counterparts.[10,19] These observations suggest that, in the absence of A′-site cations with low-lying LUMOs such as pyrazinium derivatives, the band gaps of $A'Pb_2X_6$ should be higher than those of typical 3D perovskites. A comparison of the band structures of $(dmpz)[Pb_2Br_6]$ (**1**Br) and $(CH_3NH_3)PbBr_3$, with band gaps calculated using the GW approach (see Supporting Information for computational details) and with Pb 5s orbitals aligned in energy, indeed shows that the Pb s-Pb p transition requires higher energies in $A'Pb_2X_6$ compared to $APbX_3$, due to decreased band dispersion in the former (Supporting Information, Figure S12). The band gap transition in **5**Br and **6**Br is likely a LMCT from the bromine-p band to the lead-p band, as seen in most Pb–Br perovskites. Although the conjugation in pyrazine is small, quaternization and protonation of the nitrogens are reported to decrease the LUMO energy of the dicationic pyrazinium compared to the neutral or monocationic forms.[20] The decrease of the LUMO energy has been deduced as the change in the reduction potential to more positive values for the dialkylpyrazinium cation, which is ca. + 0.9 V relative to that of pyrazine.[20a,b]

The less-distorted inorganic lattices (**3**Br and **4**Br) exhibit smaller band gaps than the more-distorted lattices (**1**Br and **2**Br). Similar to halide perovskites, this band gap modulation is likely driven by the change in dispersion of the valence bands with tilting between octahedra (or pairs of octahedra), because the conduction band (formed by the pyrazinium cations) is much less susceptible to distortion. Hence the organic molecules directly and indirectly modulate the band gap-by i) forming the conduction band, and ii) by templating distortions in the inorganic sublattice, which are reflected in the valence band.

These hybrids do not show detectable photoluminescence (PL) from the visible to the near-infrared region at ambient temperature except for **5**Br. Powdered **5**Br shows relatively broad emissions at 2.8 and 2.0 eV (Supporting Information, Figure S13). Similar dual PL bands, at both the band edge and at substantially lower energies, have been seen in lead-bromide 2D perovskites and attributed to free and self-trapped excitons, respectively.[21] The lack of PL from the pyrazinium-based lattices supports the proposed electronic structure in which the electrons and holes are located in the organic and inorganic sublattices, respectively, and therefore do not show efficient radiative recombination. PL from **4**Br becomes detectable when the temperature drops to 25 K. Upon excitation at 3.3 eV, the emission spectrum shows two

peaks: a weak emission centered at 1.6 eV (775 nm) and a stronger emission at 2.1 eV (590 nm) (Figure 5B). The photoluminescence excitation (PLE) spectrum probing the emission at 2.1 eV in **4**Br exhibits a peak above the material's absorption onset, at 3.3 eV with a shoulder at 3.1 eV (Figure 5C). We therefore tentatively assign the lower-energy emission to the band gap transition from the Hppz-based conduction band minimum (CBM) to the inorganic valence band maximum (VBM) and the higher-energy emission to the transition from the CBM + 1 state (either the Pb-6p band or the LUMO + 1 band of the Hppz cation with some Pb-6p character) to the VBM. The higher intensity of the 2.1 eV emission is consistent with greater radiative efficiency of a transition with Pb 6p→6s character. A suggested energy level diagram of **4**Br is schematically illustrated in Figure S14 (Supporting Information).

Band Structure

To further understand the redshifted absorption onsets of the expanded perovskite analogs, compared to those of analogous perovskites, we investigated the band structure of (dmpz)[Pb_2Br_6] (**1**Br) using density functional theory, with additional calculations using many-body perturbation theory in the GW approximation to compute band gaps. To calculate the band structure shown in Figure 6, we used the Heyd-Scuseria-Ernzerhof (HSE06) hybrid functional[22] as implemented in the VASP code including spin-orbit coupling (SOC) self-consistently on a $2\times2\times2$ k-point grid and with a cutoff energy for the plane wave expansion of 500 eV (the full band structure and density of states calculated using PBE + SOC is shown in Figures S15 and S16, Supporting Information). All calculations were performed with the experimental structure of **1**Br as determined from single-crystal XRD at 100 K. We find that the VBM is at $U = (\pi/a, 0, \pi/c)$, which is primarily of Br-4p/Pb-6s orbital character, similar to other lead-based halide perovskites such as $(CH_3NH_3)PbBr_3$. In stark contrast, the lowest conduction band is composed of π* orbitals of the dmpz cation and exhibits only small dispersion with the CBM at $R = (\pi/a, \pi/b, \pi/c) \approx 0.15$ eV below the highest point of the lowest-energy conduction band at $T = (0, \pi/b, \pi/c)$. This is different than the case of $(CH_3NH_3)PbBr_3$ where the lowest-energy conduction band arises from empty Pb-6p orbitals. Such Pb-6p-derived bands are found at energies much higher than the dmpz-derived conduction band in **1**Br. The HSE06 + SOC band gap of **1**Br is 1.1 eV, which underestimates the experimental gap as commonly seen for Pb-based halide perovskites.[23] Therefore, we also calculated the band gap using the GW approach, finding a value of 1.7 eV in very good agreement with experiment (see Supporting Information for computational details). We used this GW band gap (and that of $(CH_3NH_3)PbBr_3$) to scissors-shift the HSE06 + SOC energy bands in Figure 6.

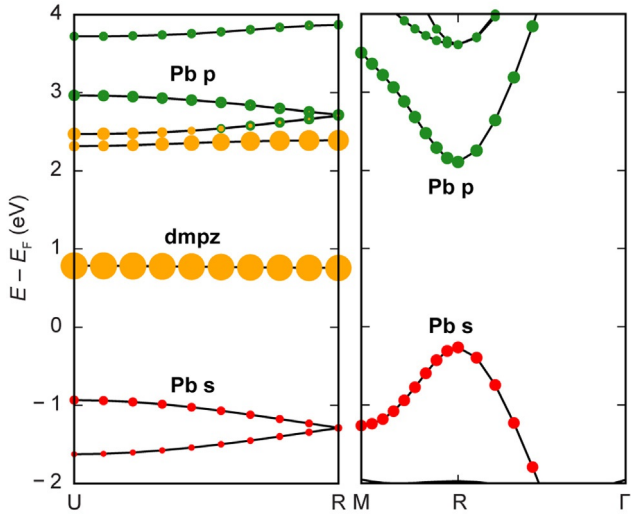

Figure 6. Band structures of **1**Br (left) and cubic $(CH_3NH_3)PbBr_3$ (right) calculated using DFT-HSE06 + SOC. Pb and dmpz orbital contributions are shown in color. Br orbital contributions are not shown for clarity. The conduction bands are shifted to match the GW band gaps (see Supporting Information). Additionally, the Pb 5s energies of both compounds have been aligned.

The small dispersion of the lowest lying conduction band originates from weak interactions between the dmpz π* and Br-4p orbitals. Such interactions are expected from the relatively small distance of 3.223(2) Å between the sp^2 carbon of the dmpz and bromide ions, which is less than the sum of van der Waals radii (3.73 Å) of these species.[24] The highest lying valence band and the conduction bands at ≈2.5–3.0 eV that show pronounced Pb-p character, are dispersive in all directions of reciprocal space, reflecting the 3D connectivity of the structure. An additional band, formed by the dmpz cations (LUMO + 1) lies only ≈0.2 eV in energy below the Pb-p bands at U. The band structure qualitatively agrees with the proposed energy level diagram in Figure S14B (Supporting Information) and explains the material's optical absorption and emission. The flat band of dmpz-based orbitals, which lies below the Pb-6p band, causes the band gap transition to take the form of a charge transfer from predominantly bromide orbitals to dmpz ions. The band structure of **1**I shares the same features with that of **1**Br (Supporting Information, Figure S17). Such an electronic structure, which facilitates charge separation across the organic-inorganic interface, has been seen in 2D perovskites that can accommodate larger aromatic molecules with low-lying π* orbitals,[5b–e] but not in 3D perovskites. By expanding the perovskite lattice, we can now access this electronic structure in a 3D lattice.

This band structure is reminiscent of that of ternary oxides of transition metals. For example, the lowest energy optical transition in the photocatalyst $BiVO_4$ arises between filled Bi 6s and O 2p states and more localized empty V 3d states.[25] Further, the magnetic order in the multiferroic perovskite $BiFeO_3$ arises from the partial occupation of localized 3d states.[26] The ability to separately synthesize and tune the energy levels and spin states of the organic molecules may provide additional control for adding magnetic moments to the lattices described here. We therefore explored methods to dope the lattices.

Doping through Organic Radicals

Because the conduction band of pyrazinium-based $A'Pb_2X_6$ retains distinct molecular character, we used the innate redox chemistry of the aromatic molecules to add electrons to the material. We prepared "doped" **1**Br (**1d**Br) by reducing 10% of the dmpz dications with cobaltocene to the radical dmpz monocations prior to the synthesis of the hybrid lattice (Figure 7A). PXRD confirmed that **1d**Br maintains the same structure as **1**Br (Supporting Information, Figure S18), suggesting that the reduced radical cation is incorporated into the structure accompanied by charge-compensating defects such as bromide vacancies, which are known to occur in bromide perovskites.[27] The 77 K electron paramagnetic resonance (EPR) spectrum of **1d**Br shows higher signal intensity than that of **1**Br, confirming the addition of unpaired electrons to the material (Figure 7B). The small EPR signature visible in **1**Br indicates that a small amount of dmpz is spontaneously oxidized during synthesis. We quantified the spin number in **1d**Br at 123 K using TEMPOL (4-hydroxy-2,2,6,6-tetramethylpiperidin-1-oxyl) as an external standard and determined that the radical concentration in **1d**Br was 0.070%, which is significant though much lower than the starting concentration for the synthesis (10%). The simulated EPR spectrum of **1d**Br, using parameters reported for the dmpz radical cation in solution, satisfactorily reproduces the experimental spectrum when including line broadening to account for the solid-state nature of the sample (Figure 7C).[28] A fit to the data gives a g of 2.008, close to the free-electron value ($g = 2.0023$), suggesting that the paramagnetic species are organic radical cations, which are as electronically isolated in solid **1d**Br as they are in solution.

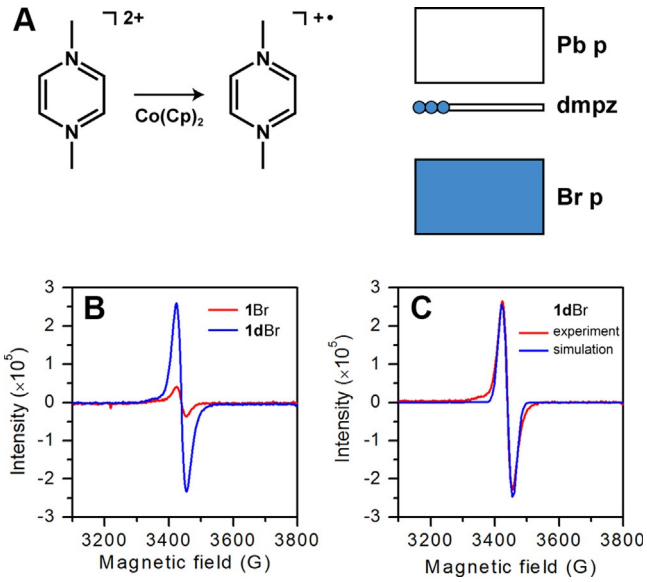

Figure 7. A) Reduction of dmpz cations by cobaltocene to populate the conduction band of (dmpz)[Pb_2Br_6] (**1**Br) with electrons to yield **1d**Br. B) Solid-state electron paramagnetic resonance (EPR) spectra of equimolar amounts of **1**Br (red) and **1d**Br (blue) at 77 K. C) Experimental (red) and simulated (blue) EPR spectra of **1d**Br at 77 K.

Certain solvents promote oxidation of the dmpz dications. For example, synthesis of **1**I in γ-butyrolactone (GBL) results in a higher radical concentration compared to the synthesis in acetonitrile, although the PXRD patterns of the products are almost identical (Supporting Information, Figure S19). The radical concentration in **1d**I was quantified to be 0.68% and a fit to the EPR spectrum of **1d**I gives a g of 2.005 with the same parameters as those of **1d**Br (Supporting Information, Figure S20). The similarity between the EPR signatures of $(dmpz)(BF_4)_2$, **1d**Br, and **1d**I (Supporting Information, Figure S21), and the correlation between the solution concentration of the radical cation and the EPR intensity (Supporting Information, Figure S22) confirm electronic doping in **1d**Br and **1d**I and indicate that the dmpz radical cations act as an electronically 0D material within the 3D inorganic lattice.

The doped materials successfully stabilize net electron spins in a semiconductor. A similar chemical approach to attain unpaired electrons in a molecular extended solid has been employed in the field of covalent-organic frameworks (COFs), enabling the formation of a paramagnetic carbon structure with high spin density.[29] A theoretical study suggests that COFs must have a narrow energy band to attain unpaired electrons with this approach.[30] Our materials can be a scaffold to attain unpaired electrons that may interact with itinerant electrons generated in the inorganic lattice.

Electrons are added to flat bands in the doped materials and are therefore not expected to show high mobility. Indeed, electronic conductivity measurements of pressed pellets of **1**I and **1d**I with graphite contacts show that **1**I is more conductive than **1d**I (Supporting Information, Figure S23A). At 378 K, **1**I exhibits a conductivity of 3.6×10^{-8} S cm^{-1}, whereas **1d**I has a conductivity of 2.1×10^{-9} S cm^{-1}. The activation energies for conductivity in **1**I and **1d**I are 0.85 and 0.64 eV, respectively (Supporting Information, Figure S23B). We speculate that carrier scattering at the charge-compensating defects (e.g., halide vacancies) in **1d**I likely result in its lower conductivity compared to **1**I despite its higher carrier number.

Conclusion

The 3D halide perovskite structure severely restricts the diversity of organic molecules that can fit within the inorganic sublattice. The expanded perovskite analogs described here afford a new structural motif that can accommodate larger organic molecules, demonstrated through the synthesis of seven new hybrid materials. Five of these materials incorporate pyrazinium derivatives and feature band structures in which the valence band comprises orbitals from the inorganic ions while the conduction band is formed entirely by orbitals from the organic cations. Thus, the lowest-energy optical transition splits charge across the organic-inorganic interface, with electrons in organic molecules and holes in the 3D Pb–X lattice. The molecular nature of the conduction band allows us to synthesize electron-doped materials by incorporating reduced radical cations in the synthesis. We expect that this hybrid electronic structure, where electrons may be trapped in flat (0D) bands and holes may be delocalized in disperse

(3D) bands may provide a tunable platform for engineering interactions between immobilized spins and itinerant electrons to yield properties such as heavy-fermion effects[31] and magnetoresistance.

Acknowledgements

This work was supported by the Department of Energy, Office of Basic Energy Sciences, Division of Materials Sciences and Engineering, under contract DE-AC02-76SF00515. D.U. thanks the Japanese Society for the Promotion of Science for a postdoctoral fellowship (JSPS Overseas Research Fellowship). B.A.C. is supported by an NSF graduate fellowship (DGE-114747). M.A.M. was supported by fellowships from the Center for Molecular Analysis and Design, the National Science Foundation (NSF; DGE-114747), and Stanford's Diversifying Academia, Recruiting Excellence (DARE) Program. We thank Dr. Matthew D. Smith for experimental assistance and Prof. E. I. Solomon for access to equipment. Part of this work was performed at the Stanford Nano Shared Facilities (SNSF), supported by the NSF under award ECCS-1542152. DFT calculations supported by the Department of Energy, Office of Basic Energy Sciences, Division of Materials Sciences and Engineering (Theory FWP), under contract No. DE-AC02-05CH11231. Computational resources used at the Molecular Foundry were supported by the Department of Energy, Office of Basic Energy Sciences, under contract No. DE-AC02-05CH11231. L.L. acknowledges partial support by the Feodor-Lynen program of the Alexander-von-Humboldt foundation, the Research Network Solar Technologies go Hybrid (SolTech), the Elite Network Bavaria, and the German Research Foundation (DFG) through SFB840.

Conflict of interest

The authors declare no conflict of interest.

Keywords: 3D halide perovskite analogs · charge separation · lattice expansion · radical doping

[1] C. Sanchez, G. J. de A. A. Soler-Illia, F. Ribot, T. Lalot, C. R. Mayer, V. Cabuil, *Chem. Mater.* **2001**, *13*, 3061 – 3083.
[2] T. Asefa, M. J. Maclachlan, N. Coombs, G. A. Ozin, *Nature* **1999**, *402*, 867 – 871.
[3] a) O. M. Yaghi, M. O'Keeffe, N. W. Ockwig, H. K. Chae, M. Eddaoudi, J. Kim, *Nature* **2003**, *423*, 705 – 714; b) S. Kitagawa, R. Kitaura, S. Noro, *Angew. Chem. Int. Ed.* **2004**, *43*, 2334 – 2375; *Angew. Chem.* **2004**, *116*, 2388 – 2430; c) L. J. Murray, M. Dincă, J. R. Long, *Chem. Soc. Rev.* **2009**, *38*, 1294 – 1314.
[4] a) D. B. Mitzi, *J. Chem. Soc. Dalton Trans.* **2001**, 1 – 12; b) M. D. Smith, E. J. Crace, A. Jaffe, H. I. Karunadasa, *Annu. Rev. Mater. Res.* **2018**, *48*, 111 – 136.
[5] a) M. Era, K. Maeda, T. Tsutsui, *Chem. Lett.* **1997**, *26*, 1235 – 1236; b) M. Era, K. Maeda, T. Tsutsui, *Chem. Phys. Lett.* **1998**, *296*, 417 – 420; c) D. B. Mitzi, K. Chondroudis, C. R. Kagan, *Inorg. Chem.* **1999**, *38*, 6246 – 6256; d) M. Braun, W. Tuffentsammer, H. Wachtel, H. C. Wolf, *Chem. Phys. Lett.* **1999**, *303*, 157 – 164; e) M. Braun, W. Tuffentsammer, H. Wachtel, H. C. Wolf, *Chem. Phys. Lett.* **1999**, *307*, 373 – 378; f) M. Era, A. Shimizu, *Mol. Cryst. Liq. Cryst. Sci. Technol. Sect. A* **2001**, *371*, 199 – 202; g) X.-H. Zhu, N. Mercier, P. Frère, P. Blanchard, J. Roncali, M. Allain, C. Pasquier, A. Riou, *Inorg. Chem.* **2003**, *42*, 5330 – 5339; h) K. Sakai, T. Sonoyama, T. Tsuzuki, M. Ichikawa, Y. Taniguchi, *Chem. Lett.* **2005**, *34*, 212 – 213; i) C. Liu, W. Huhn, K.-Z. Du, A. Vazquez-Mayagoitia, D. Dirkes, W. You, Y. Kanai, D. B. Mitzi, V. Blum, *Phys. Rev. Lett.* **2018**, *121*, 146401.
[6] a) D. Weber, *Z. Naturforsch. B* **1978**, *33*, 1443 – 1445; b) C. C. Stoumpos, C. D. Malliakas, M. G. Kanatzidis, *Inorg. Chem.* **2013**, *52*, 9019 – 9038.
[7] a) W. Peng, X. Miao, V. Adinolfi, E. Alarousu, O. El Tall, A.-H. Emwas, C. Zhao, G. Walters, J. Liu, O. Ouellette, J. Pan, B. Murali, E. H. Sargent, O. F. Mohammed, O. M. Bakr, *Angew. Chem. Int. Ed.* **2016**, *55*, 10686 – 10690; *Angew. Chem.* **2016**, *128*, 10844 – 10848; b) A. D. Jodlowski, C. Roldán-Carmona, G. Grancini, M. Salado, M. Ralaiarisoa, S. Ahmad, N. Koch, L. Camacho, G. De Miguel, M. K. Nazeeruddin, *Nat. Energy* **2017**, *2*, 972 – 979.
[8] a) B. Saparov, D. B. Mitzi, *Chem. Rev.* **2016**, *116*, 4558 – 4596; b) M. D. Smith, B. A. Connor, H. I. Karunadasa, *Chem. Rev.* **2019**, *119*, 3104 – 3139.
[9] M. P. Shores, L. G. Beauvais, J. R. Long, *J. Am. Chem. Soc.* **1999**, *121*, 775 – 779.
[10] a) G. Zheng, Y. Li, J. Lin, C. Lin, *Cryst. Growth Des.* **2008**, *8*, 1990 – 1996; b) C. J. Que, C. J. Mo, Z. Q. Li, G. L. Zhang, Q. Y. Zhu, J. Dai, *Inorg. Chem.* **2017**, *56*, 2467 – 2472.
[11] a) H.-Y. Zhang, X.-J. Song, H. Cheng, Y.-L. Zeng, Y. Zhang, P.-F. Li, W.-Q. Liao, R.-G. Xiong, *J. Am. Chem. Soc.* **2020**, *142*, 4604 – 4608; b) X. Li, Y. He, M. Kepenekian, P. Guo, W. Ke, J. Even, C. Katan, C. C. Stoumpos, R. D. Schaller, M. G. Kanatzidis, *J. Am. Chem. Soc.* **2020**, *142*, 6625 – 6637.
[12] K. S. Prasad, T. J. Curphey, *J. Org. Chem.* **1972**, *37*, 2259 – 2266.
[13] I. C. Smith, E. T. Hoke, D. Solis-Ibarra, M. D. Mcgehee, H. I. Karunadasa, *Angew. Chem. Int. Ed.* **2014**, *53*, 11232 – 11235; *Angew. Chem.* **2014**, *126*, 11414 – 11417.
[14] A. S. Chia, R. F. Trimble, *J. Phys. Chem.* **1961**, *65*, 863 – 866.
[15] N. Ahn, D.-Y. Son, I.-H. Jang, S. M. Kang, M. Choi, N.-G. Park, *J. Am. Chem. Soc.* **2015**, *137*, 8696 – 8699.
[16] L. Katz, R. Ward, *Inorg. Chem.* **1964**, *3*, 205 – 211.
[17] J. L. Knutson, J. D. Martin, D. B. Mitzi, *Inorg. Chem.* **2005**, *44*, 4699 – 4705.
[18] a) L. A. Vermeulen, M. E. Thompson, *Nature* **1992**, *358*, 656 – 658; b) Z. Tang, A. M. Guloy, *J. Am. Chem. Soc.* **1999**, *121*, 452 – 453; c) J. Fujisawa, T. Ishihara, *Phys. Rev. B* **2004**, *70*, 113203; d) N. Mercier, *Eur. J. Inorg. Chem.* **2013**, 19 – 31.
[19] L. Mao, P. Guo, M. Kepenekian, I. Hadar, C. Katan, J. Even, R. D. Schaller, C. C. Stoumpos, M. G. Kanatzidis, *J. Am. Chem. Soc.* **2018**, *140*, 13078 – 13088.
[20] a) L. N. Klatt, R. L. Rouseff, *J. Am. Chem. Soc.* **1972**, *94*, 7295 – 7304; b) W. Kaim, *Heterocycles* **1985**, *23*, 1363 – 1366; c) M. C. Monteiro, K. C. F. Toledo, B. M. Pires, R. Wick, J. A. Bonacin, *Eur. J. Inorg. Chem.* **2017**, 1979 – 1988.
[21] M. D. Smith, A. Jaffe, E. R. Dohner, A. M. Lindenberg, H. I. Karunadasa, *Chem. Sci.* **2017**, *8*, 4497 – 4504.
[22] J. Heyd, G. E. Scuseria, M. Ernzerhof, *J. Chem. Phys.* **2003**, *118*, 8207 – 8215.
[23] L. Leppert, T. Rangel, J. B. Neaton, *Phys. Rev. Mater.* **2019**, *3*, 103803.
[24] M. D. Prasanna, T. N. Guru Row, *Cryst. Eng.* **2000**, *3*, 135 – 154.
[25] A. Walsh, D. J. Payne, R. G. Egdell, G. W. Watson, *Chem. Soc. Rev.* **2011**, *40*, 4455 – 4463.
[26] R. Ramesh, N. A. Spaldin, *Nat. Mater.* **2007**, *6*, 21 – 29.
[27] A. H. Slavney, L. Leppert, A. Saldivar Valdes, D. Bartesaghi, T. J. Savenije, J. B. Neaton, H. I. Karunadasa, *Angew. Chem. Int.*

Ed. **2018**, *57*, 12765 – 12770; *Angew. Chem.* **2018**, *130*, 12947 – 12952.
[28] a) D. R. Eaton, J. M. Watkins, R. J. Buist, *J. Am. Chem. Soc.* **1985**, *107*, 5604 – 5609; b) S. Stoll, A. Schweiger, *J. Magn. Reson.* **2006**, *178*, 42 – 55.
[29] E. Jin, M. Asada, Q. Xu, S. Dalapati, M. A. Addicoat, M. A. Brady, H. Xu, T. Nakamura, T. Heine, Q. Chen, D. Jiang, *Science* **2017**, *357*, 673 – 676.
[30] H. Yu, D. Wang, *J. Am. Chem. Soc.* **2020**, *142*, 11013 – 11021.
[31] "Heavy Fermions: Electrons at the Edge of Magnetism": P. Coleman in *Handbook of Magnetism and Advanced Magnetic Materials*, *Vol. 1* (Eds.: H. Kronmüller, S. Parkin), Wiley, Chichester, **2007**, pp. 95 – 148.

Manuscript received: April 7, 2020
Accepted manuscript online: July 10, 2020
Version of record online: August 26, 2020

